ADVANCED MATERIALS INTERFACES
Open Access
www.advmatinterfaces.de

An Advanced Healthcare Sensing Platform for Direct Detection of Viral Proteins in Seconds at Femtomolar Concentrations via Aerosol Jet 3D-Printed Nano and Biomaterials

Md. Azahar Ali, George Fei Zhang, Chunshan Hu, Bin Yuan, Shou-Jiang Gao, and Rahul Panat**

Sensing of viral antigens has become a critical tool in combating infectious diseases. Current sensing techniques have a tradeoff between sensitivity and time of detection; with 10–30 min of detection time at a relatively low sensitivity and 6–12 h of detection at a high (picomolar) sensitivity. In this research, uniquely nanoengineered interfaces are demonstrated on 3D electrodes that enable the detection of spike antigens of SARS-CoV-2 and their variants in seconds at femtomolar concentrations with excellent specificity, thus, overcoming this tradeoff. The 3D electrodes, manufactured using a high-resolution aerosol jet 3D nanoprinter, consist of a microelectrode array of sintered gold nanoparticles coated with graphene and antibodies specific to severe acute respiratory syndrome coronavirus-2 (SARS-CoV-2) spike antigens. An impedance-based sensing modality is employed to sense several pseudoviruses of SARS-CoV-2 variants of concern (VOCs). This device is sensitive to most of the pseudoviruses of SARS-CoV-2 VOCs. A high sensitivity of 100 fM, along with a low limit-of-detection of 9.2 fM within a test range of 0.1–1000 pM, and a detection time of 43 s are shown. This work illustrates that effective nano-bioengineering of interfaces can be used to create an ultrafast and ultrasensitive healthcare diagnostic tool for combating emerging infections.

1. Introduction

Pathogenic infections are responsible for a host of ailments that affect human health and cause millions of deaths around the world each year.[1] This is complicated by the fact that emerging infectious diseases and their variants continue to emerge, such as in the case of the recent outbreaks of the severe acute respiratory syndrome coronavirus-2 (SARS-CoV-2) and its variants of concern (VOCs).[2] Rapid and early detection of infections is critical for healthcare management and control. A number of diagnostic tools such as CRISPR-Cas systems,[3] immunoassays,[4] serological,[5] lateral flow,[6] loop-mediated isothermal amplification,[7] colorimetry,[8] and reverse transcription-quantitative polymerase chain reaction-PCR (or RT-qPCR)[9] have been reported to detect pathogens and their variants with different sensitivities and specificities.[10] However, a tradeoff exists between the needs for a highly sensitive detection (e.g., via RT-qPCR) that takes 6–12 h; and a rapid, 10–30 min, antigen test that has a low sensitivity and hence cannot detect infection at an early stage. Moreover, only one VOC can be detected at a time by using these diagnostics tools. For example, the detection of a specific SARS-CoV-2 VOC is realized by an individual test including a RT-qPCR test. Due to these tradeoffs and

M. A. Ali, C. Hu, B. Yuan, R. Panat
Department of Mechanical Engineering
Carnegie Mellon University
Pittsburgh, PA 15213, USA
E-mail: rpanat@andrew.cmu.edu

The ORCID identification number(s) for the author(s) of this article can be found under https://doi.org/10.1002/admi.202400005

[Correction added on March 13, 2024, after first online publication: the affiliation of the fifth author has been updated in this version.]

DOI: 10.1002/admi.202400005

M. A. Ali
School of Animal Sciences
Virginia Tech
Blacksburg, VA 24061, USA

G. F. Zhang, S.-J. Gao
Cancer Virology Program
UPMC Hillman Cancer Center and Department of Microbiology and Molecular Genetics
University of Pittsburgh School of Medicine
Pittsburgh, PA 15213, USA
E-mail: gaos8@upmc.edu

limitations, these tools cannot give results on the spot, require longer testing times, and have limited sensitivity and accuracy.

SARS-CoV-2 VOCs primarily caused by the genetic mutation in the spike protein continue to emerge around the world.[2] They are responsible for the continuation of the COVID-19 pandemic for over 3.5 years due to their increased viral transmission, pathogenicity, and ability to evade the vaccine.[11] Throughout the pandemic, five major VOCs were reported by the World Health Organization (WHO) including *B.1.1.7* (Alpha), *B.1.351*, (Beta), *P.1* (Gamma), *B.1.617.2* (Delta), and *B.1.1.529* (Omicron) that evolved from the SARS-CoV-2 wild-type (WT) strain.[12] Compared to the original virus, most VOCs can be more rapidly transmitted.[13] For example, the *B.1.1.7* (Alpha) variant is 43%–90% more contagious causing 61% more mortality compared to the predecessor lineage.[14] The *B.1.617.2* (Delta) variant led a second wave of infectivity in India which caused over 300 000 new cases per day and spread rapidly across the globe.[15] Importantly, there is no specific vaccine that can neutralize all the SARS-CoV-2 VOCs.[16]

Pseudovirus containing specific SARS-CoV-2 spike proteins are useful in studying viral infectivity, vaccine development, pathogenesis, and diagnosis of VOCs.[2a,17,18] It is known that the spike glycoprotein mediates virus entry into the susceptible cells by binding to the human angiotensin-converting enzyme 2 (hACE2) receptor.[2a] As the pseudotyped viruses could serve as alternative viruses to study the SARS-CoV-2 variants,[19] we have utilized the pseudoviruses derived from SARS-CoV-2 VOCs to test biosensor performances.

1D and 2D nanomaterial-based biosensors were exploited to detect SARS-CoV-2 with limited performance gains.[20,21] Numerous sensors used materials such as Ti_3C_2-MXene nanosheets,[22] single strand DNA capped gold nanoparticles,[23] aptamer-decorated solid-state nanopores,[24] platinum decorated MoS_2 sheets,[25] field-effect transistors,[25] nanoporous structures,[26] and graphene[27] to detect SARS-CoV-2 with improved sensitivities. Despite these improvements, there is no practical device that can detect SARS-CoV-2 infections in seconds. To overcome these limitations, we recently introduced an additively manufactured healthcare device using Aerosol Jet 3D nanoprinting with engineered interfaces.[28] This approach allows the manufacture of hierarchical multi-length-scale 3D structures as electrodes[28a] with their surfaces coated with nanoscale graphene and biomolecules combined with a microfluidic device. This geometry accelerates the interaction of the target molecules with the electrode at very low concentrations.[28,29] The resulting sensor has the potential for ultra-high sensitivity, selectivity, femtomole-level limit-of-detection, with a good reproducibility; and thus, an ability to break the tradeoff between the diffusion-limited time-of-detection and sensitivity. Such an interface-engineered platform can then be used for the detection of specific antigens for SARS-CoV-2 VOCs. Such geometries have been used to quantify biomarkers such as antibodies in our previous work,[28b,29] but not for direct viral detection.

In this study, we demonstrate an advanced healthcare platform for biosensing that enables the detection of proteins of SARS-CoV-2 VOCs (i.e., antigens of VOCs) in seconds at ultra-low (femtomolar) concentrations, thereby overcoming the tradeoff between the time-of-detection and sensitivity for sensing of pathogens. Sensing of viral proteins of VOCs in seconds has significant positive implications for the management of global health issues caused by pathogenic diseases. This healthcare platform was realized by an array of gold micropillars functionalized with graphene and antibodies specific to the SARS-CoV-2 spike S1 protein. Low limit-of-detection (9.2 fM), high analytical sensitivity (100 fM), rapid detection (43 s) and high selectivity were demonstrated for this 3D printed biosensor. The sensor manifests excellent performance with a number of pseudotyped viruses of SARS-CoV-2 VOCs without any multiplex functionality of the device.

2. Experimental Section

The biosensing platform used in this work was constructed by 3D printing of the working electrode in an electrochemical cell and then coating the electrodes with appropriate antibodies specific to SARS-CoV-2 spike proreins. The materials and methods are discussed below.

2.1. Chemicals and Materials

The chemicals EDC (1-ethyl-3-(3-dimethylaminopropyl) carbodiimide hydrochloride), NHS (N-hydroxysuccinimide), sodium carbonate, sodium bicarbonate, bovine serum albumin (BSA) used in this work were obtained from Sigma–Aldrich (Burlington, MA). The polydimethylsiloxane (SYLGARD 184 Silicone Elastomer Kit) required for the microfluidic channel of the sensor was obtained from Dow Corning (Midland, MI). To manufacture the 3D microelectrode array using aerosol jet 3D printing, a gold (Au) nanoparticle ink was used (UTDAu40, UT Dots Inc., Champaign, IL). The average gold particle size was ≈5 nm, the nanoparticle loading in the ink was 40% (wt) and the ink viscosity was ≈3 cP. The human recombinant SARS-CoV-2 spike S1-His protein, Interleukin-6 (IL-6), SARS-CoV-2 nucleocapsid, interferon (IFN)-α, -β and -γ, and SARS-CoV-2 spike S1 antibody are purchased from the Sino Biological US Inc. (Wayne, PA). SARS-CoV-2 spike S1 protein with serial dilutions at 1000, 100, 10, 1, and 0.1 pM were used for the sensor calibration. Once solutions were prepared and aliquoted, these solutions were stored at −20 °C before their use. Further, the pseudoviruses of SARS-CoV-2 WT and VOCs were utilized to evaluate the sensing performance.

2.2. Cells and Culture Condition

Human embryonic kidney epithelial-like cell HEK293T (CRL-3216, ATCC) was used for packaging pseudoviruses of SARS-CoV-2 WT and VOCs. HEK293T cell line was maintained in Dulbecco's Modified Eagle Medium (DMEM) with 10% FBS and 1% Penicillin/Streptomycin 100 × Solution.

2.3. Construction of Plasmids

Plasmids SARS-CoV-2 spike proteins of VOCs were constructed as previously reported.[30] In brief, the reporter plasmid pNL4-3.Luci.R-.E- expressing the firefly gene was used to clone the

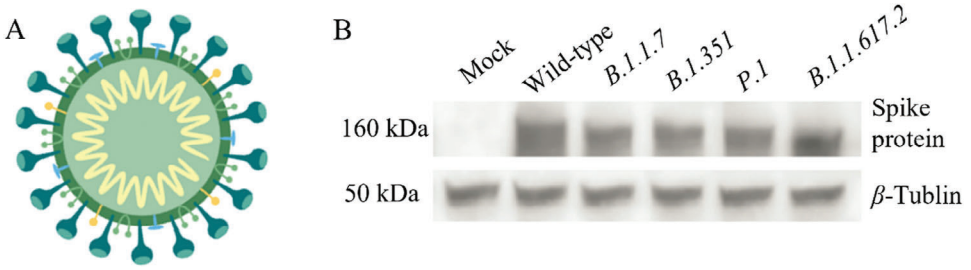

Figure 1. Packaging of pseudoviruses SARS-CoV-2 VOCs. A) Structure of SARS-CoV-2 and spike. B) The expression of SARS-CoV-2 spike proteins was confirmed by Western-blotting.

backbone of the virus.[30] Plasmids expressing S proteins of SARS-CoV-2 WT and VOCs were generous gifts from Dr. David Nemazee (The Scripps Research Institute, La Jolla, CA).[31] The S protein genes were cloned into pcDNA3.1(+) by restriction digestion and T4 ligation. The expression of the S protein was confirmed by Western-blotting as previously described.[30]

2.4. Packaging of Pseudoviruses

Pseudoviruses used were packaged as previously described.[30] In this study, the SARS-CoV-2 WT and VOCs were packaged (**Figure** 1A). For this, two specific plasmids were transfected into HEK293T cells. pcDNA3.1(+) was acted as a negative control. A plasmid expressing vesicular stomatitis virus glycoprotein (VSVG) was used to package the pseudovirus and used as a heterogenous control. The expression of spike proteins of SARS-CoV-2 were confirmed by Western-blotting (Figure 1B).

2.5. SDS-PAGE and Western-Blotting

Sodium dodecyl sulfate polyacrylamide gel electrophoresis (SDS-PAGE) and Western-blotting were conducted to determine the expression and reactivities of the antibodies of spike proteins. Experiments were conducted as previously described.[30,32] Briefly, cells transfected with plasmids expressing the spike proteins or the control plasmid were lysed. Samples were loaded and analyzed by SDS-PAGE. Protein samples on gel were transformed onto nitrocellulose (NC) membranes with a transfer system (Bio-Rad). Western-blotting assay was performed according to the published study (Figure 1B).[21] Membrane containing protein samples were blocked with 5% nonfat milk for 1 h at room temperature (RT, 25 °C). The membrane was incubated with antibodies to SARS-CoV-2 spike proteins (Sino Biological) in 1% BSA at 4 °C overnight (≈16 h). Membrane was washed three times in TBST solution. Membrane was incubated with HRP tagged anti-rabbit secondary antibody for 1 h at RT. Membrane was incubated with SuperSignal West Femto Maximum Sensitivity Substrate (34 096, Thermo Fisher Scientific) and the signal detected with the ChemiDocTM MP Imaging System (Bio-Rad).

3. Device Design and Manufacturing

Figure 2A shows the schematic illustration of the 3D nano-printed device for the detection of SARS-CoV-2 spike S1 antigen.

3.1. Sensor Cell Design

The sensor has two major parts: a) a three electrode-based (WE = working electrode; CE = counter electrode and RE = reference electrode) electrochemical system, and b) a PDMS-based microfluidic device. The electrochemical electrodes along with a 3D microelectrode array were made of 3D nano-printing and e-beam evaporation whereas the PDMS-based microfluidics was fabricated using a micromachining technique. Details of device manufacturing were previously described.[29] In brief, the device design was first developed using the AutoCAD software. A Kapton tape-based shadow mask was fabricated using an automated cutter (Silhouette Curio, Silhouette America, Inc., Lindon, UT). The shadow mask was placed on a glass substrate to coat layers of chromium (Cr; 10 nm) and gold (Au; 100 nm). The Cr layer acted as an adhesive layer. The metal coating was performed by an e-beam evaporator (Kurt Lesker PVD 75, Jefferson Hills, PA).

In this design, the area of the WE was set to 2 mm × 2 mm where the 3D array of micropillar electrodes was manufactured (Figure 2A). The CE is chosen as a bare Au layer. For the RE a thin layer (1 μm thick) of silver/silver chloride ink (Ercon, Inc. Wareham, MA) was coated on top of the Au layer by placing another shadow mask and was dried at 150 °C for 2 h to remove the solvent. This step was done once we printed the gold micropillars.

To control the biological fluids, a PDMS-based microfluidic device was made to integrate the three-electrode system.[29] This was realized by a soft-replica molding method. A high-precision milling machine was used to create a polymethylmethacrylate (PMMA) mold. This PMMA mold has channel depth of 1 mm, width of 2 mm, and length of 20 mm. A PDMS solution was prepared by mixing it with a curing agent (crosslinker) at a ratio of 10:1 and poured on the PMMA channel to generate an opposite pattern. The bubbles were eliminated by degassing for 1 h (10^{-4} Torr) in a vacuum chamber and cured at 80 °C for 2 h. PDMS was then peeled off from PMMA substrate. The opposite pattern of PDMS was then poured with PDMS solution. A silicone oil (Ease Release 205, Reynoldsam Advanced Materials, Macungie, PA) was spread on top PDMS mold before this step. After curing at 80 °C for 2 h, we peeled off the resulting PDMS channel from the mold. Holes were created by punching with a hollow needle at two ends of the channels where Tygon tubes were inserted to introduce the fluid containing the analyte. For measurements, this PDMS channel was placed on top of the electrodes.

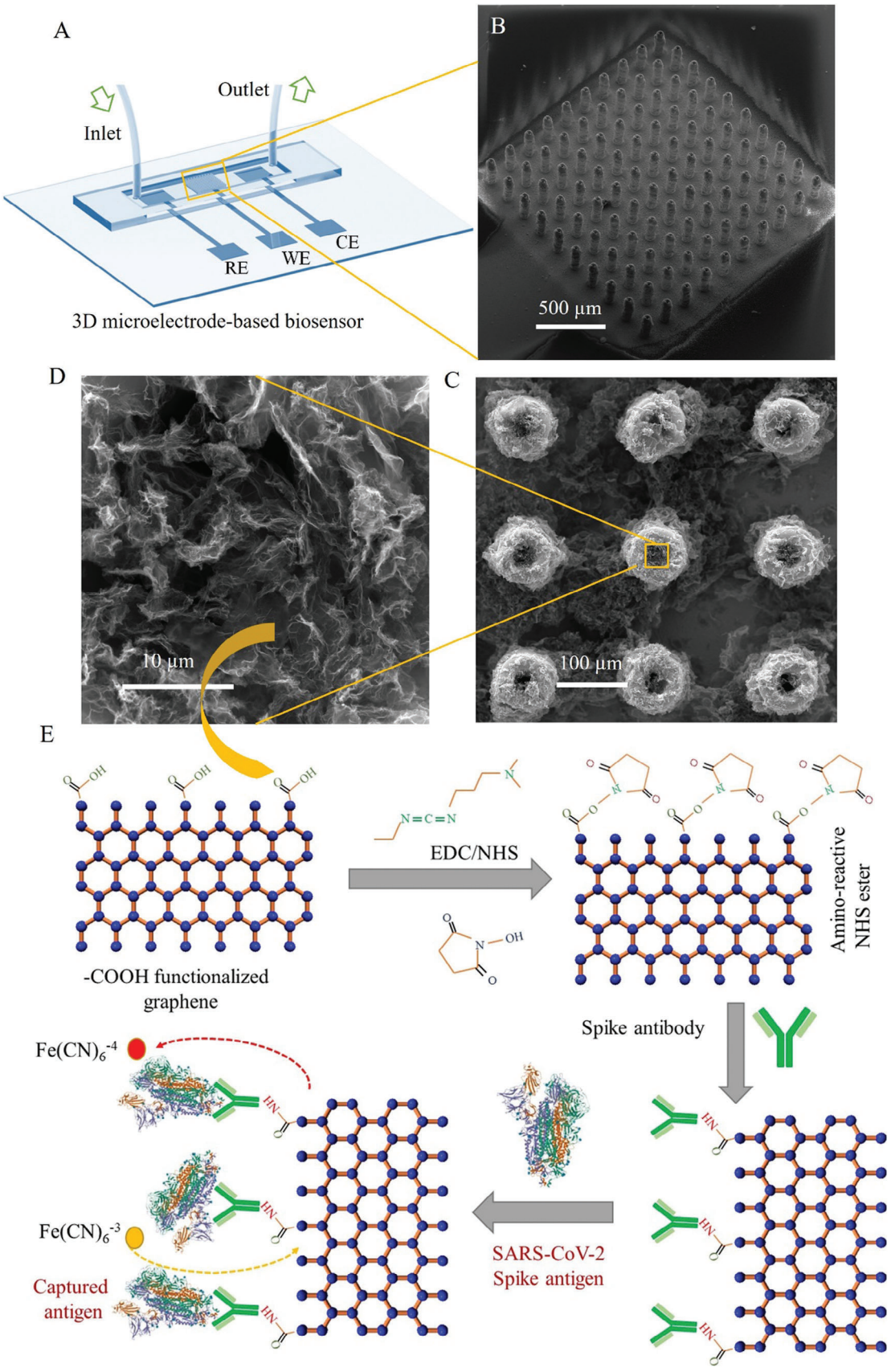

3.2. 3D Nano-Printing

The WE of the sensor (2 × 2 mm^2) was made of Au micropillars fabricated using aerosol jet 3D nano-printing and sintering of gold nanoparticles (Au NPs). An array (10 × 10) of micropillar electrodes was manufactured. Details of 3D manufacturing of the array is described in reported article.[29] In brief, an array (10 × 10) of micropillars was printed using an aerosol jet 3D printer (Model AJ-300, Optomec, Inc., Albuquerque, NM, USA). The printer has a deposition head along with a printing nozzle, an ultrasound source to create aerosolized particles, a movable stage (X-Y direction), and a shutter. In this printing, the size of gold nanoparticles, viscosity, and density in the ink were 2–5 nm, 3 cP, and 40 wt%, respectively. These particles were dispersed in an organic non-polar solvent and loaded into the vial (1 mL solution). A nozzle of diameter of 150 µm was chosen to control the printing line width of 15–20 µm. Before printing, the sensor was designed using AutoCAD software (AutoCAD 2020, Autodesk Inc., San Rafael, CA, USA) and converted into a "prg" file. Ultrasound energy was applied to the ink to form aerosolized micron-sized droplets. These droplets were carried to the printing nozzle with the help of carrier gas (nitrogen, N_2) with a pressure of 24 sccm. Further, a sheath gas (N_2) was applied at a pressure of 60 sccm to focus the beam of droplets aerodynamically on the substrate. Platen temperature was maintained at 100 °C. Once a layer was printed, the solvent evaporated due to the heat from the platen. Because of high surface tension for the micron-scale particles, layer-by-layer printing was possible. Each layer of the toroid-shaped ring forming a micropillar was 5–10 µm thick. The printed aerosol droplets of nanoparticles were sintered at 400 °C for 5 h to remove the binders and solvents from the pillars. The resulting array of micropillars is shown in Figure 2B. In this study, the pillar height, pillar diameter, and pillar-to-pillar distance were set to ≈250, ≈70, and ≈118 µm, respectively. Based on COMSOL simulation in our previous studies,[29] we have chosen an optimum array size of 10 × 10 to construct this sensing platform.

3.3. Array Functionalization

Before coating of viral (SARS-CoV-2) antibodies, the microelectrode array was functionalized with reduced graphene oxide (rGO) flakes. The rGO coating on the Au surface is an important step that enhances the loading of antibodies on the 3D surface of the Au pillar. For this, the powder form of rGO sheets (ACS Materials LLC, Pasadena, CA) was dispersed into DI water (0.2 mg mL^{-1}) and sonicated for 2 h. To coat rGO, a PDMS fence was placed surrounding the Au array and 20 µL of rGO solution was drop-cast and dried at 80 °C. rGO sheets are seen to adhere to the micro-texture of the Au pillar surface due to electrostatic interaction between them. Figure 2C,D shows the rGO coating on the surface of the Au pillar.

A step-wise functionalization process of rGO-Au micropillar with antibodies specific to SARS-CoV-2 spike proteins is shown in Figure 2E. A coupling reagent was prepared with EDC (0.2 M) and NHS (0.05 M) at 1:1 ratio and was spread on rGO-Au micropillar array. The EDC-NHS treatment on the rGO activates the —COOH functional groups and allows covalent binding with antibodies. The coated rGO was used as a transducer material due to its excellent properties.[33] They have excellent high electron transfer, high surface area, functionality, and tuning electrochemical properties.[34] In this study, an IgG spike S1 antibody to SARS-CoV-2 was used to functionalize on the surface of the rGO-Au array to detect spike S1 antigens via impedance transduction. The abundant functional groups of rGO (—COOH, —CHO, —OH)[35] enable covalent conjugation of spike S1 antibodies. A 20 µL solution (5 µg mL^{-1}) of spike S1 antibodies was used for drop-casting over the rGO-Au electrode in a humid condition for 4 h. This covalent binding between —COOH groups of rGO and —NH_2 of antibodies resulted in strong amide bonds (C—N) on the sensor surface.[36] This is due to an amidation reaction occurring on the sensor surface. In reaction chemistry, the EDC activates the —COOH groups of rGO, while NHS acts as a stabilizer. Further, a 20 µL of BSA solution (2 mg mL^{-1}) was introduced to the sensor surface to block any non-specific sites of the antibody functionalized rGO-Au micropillar. This array of microelectrodes act as sensitive immuno-detectors for COVID-19 antigens without any labeling agents.

3.4. Device Assembly

Once the array-electrode in the sensor was functionalized, a PDMS-based microfluidic channel was integrated with the sensor . Tygon tubes were used to connect with the PDMS channel and a syringe to control biofluids. The WE, RE and CE pads in this sensor were connected to a commercial potentiostat (VersaSTAT 3, AMETEK. Inc.) using copper adhesive tapes.

For this study, the volume of the microfluidic channel is set to 30 mm^3. The liquid needed to fill the microfluidic channel is ≈30 µL. A fingerprick with 3 drops of sample (i.e., blood) is about 5–10 uL, thus we may need a dilution of real samples by 3–6× using a buffer solution.

4. Results

4.1. Electrochemical Characterization

An electrochemical impedance spectroscopy (EIS) measurement was conducted to investigate the electrochemical properties of

Figure 2. 3D nano-printed sensor for rapid detection of SARS-CoV-2 VOCs. A) Schematic presentation of a 3D nano-printed sensor. The device consists of three electrodes such as working, counter, and reference wherein the working electrode was made of an array of micropillars of gold nanoparticles. This array was manufactured by an Aerosol Jet 3D nanoparticle printer. B) SEM image of the nano-printed micropillar array. C,D) SEM images of graphene coating on the gold microelectrode array (graphene-Au). The zoomed-in SEM image (D) shows the assembly of wrinkled graphene on the tip of a micropillar. E) Stepwise representation of the surface functionalization to coat the SARS-CoV-2 spike S1 antibodies on rGO-Au via a unique EDC-NHS conjugation chemistry. In reaction chemistry, the EDC activates the -COOH groups of graphene, while NHS acts as a stabilizer. The amide bonds were formed between spike S1 antibodies and the graphene-Au surface. Captured antigens by antibodies specific to SARS-CoV-2 spike proteins on the rGO-Au microelectrode hinder the electron transfer due to oxidation, thus enhancing the electrode impedance.

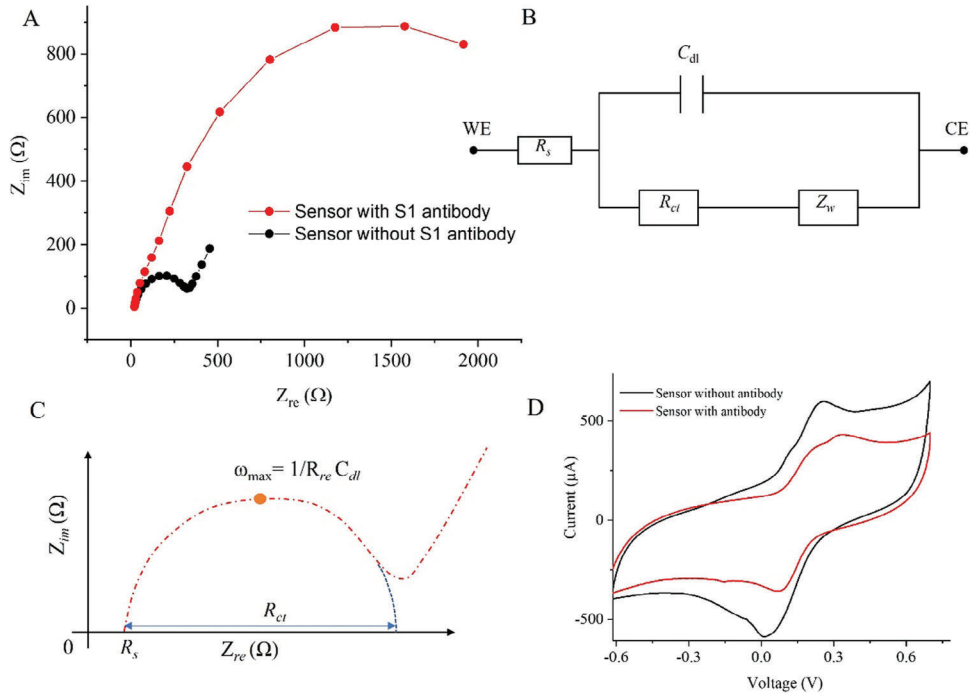

Figure 3. Sensor characterization. A) Electrochemical impedance spectroscopy (EIS) measurements show the Nyquist plots of the sensor. The sensor's electrode (rGO-Au) was functionalized with SARS-CoV-2 spike S1 antibodies before and after measurements. B) Schematic illustration of an equivalent circuit between the counter and working electrodes. R_{ct} is the charge transfer resistance, R_s is the solution resistance, C_{dl} is double-layer capacitance and Z_w is the Warburg resistance. C) The diameter of the semicircle shown in a typical Nyquist plot is the R_{ct}. An AC signal with an amplitude of 1.0 mV and a fixed frequency range (10 000–1 Hz) was applied to conduct the EIS experiments. D) The cyclic voltammetry (CV) of the sensor was conducted with and without spike S1 antibodies. With antibody coating, the sensor current is decreased due to blocking of electrons by antibodies on the electrode surface. Both EIS and CV measurements were performed in presence of PBS (50 mM) mixed with a ferro/ferricyanide (5 mM) redox mediator.

the sensor. We note that EIS is a suitable tool to study the interfacial properties related to the antibody–antigen interactions occurring at the electrode surface.[37] **Figure 3A** depicts the Nyquist plot of the 3D sensor with and without spike S1 antibodies. The charge transfer resistances are the diameter values of semicircles of the Nyquist plots, and it is denoted by R_{ct}. This R_{ct} value is varies with the rate of faradaic reaction at the electrode and amount of capturing of proteins on the electrode surface during detection. A Randles equivalent circuit shown in Figure 3C consists of a solution resistance (R_s) in series with a parallel double-layer capacitance (C_{dl}) and R_{ct} plus Warburg resistance (Z_w). The sensor with antibodies (anti-S1/rGO-Au array) showed a 7.8 times higher value of R_{ct} (2.55 kΩ) compared to the sensor without antibodies (rGO-Au array; R_{ct} ≈0.327 kΩ). This is because of the decoration of antibodies specific to the spike protein on the rGO-Au surfaces of the 3D electrodes which impede the electron transfer from an electrolyte to the impedance collector electrode.

In addition to the EIS study, we also carried out the cyclic voltammetry (CV) measurements of the 3D rGO-Au microelectrode array sensor with and without antibody functionalization. We note that CV is a simple, and fast technique to study the qualitative and quantitative information on redox reactions. As shown in Figure 3D, this 3D biosensor with a microelectrode array shows distinct oxidation and reduction peaks due to a redox reaction of the ferro/ferricyanide mediator. The level of oxidation current of the sensor with antibodies is decreased by 1.4 times (Figure 3D). The layer of antibodies along with BSA molecules on the sensor surface blocks the electron transfer from the electrolyte to a current collector. This is due to the intrinsic insulating behavior of antibodies and BSA molecules which blocks the electron acceleration toward the current collector.[35b] The electrode area for both sensors was kept at 0.104 cm^2. The diffusion coefficient for both 3D rGO-Au microelectrode array sensors without and with antibodies and BSA are calculated as 184.9 and 95.2 $\mu cm^2\ s^{-1}$, respectively.[38] The peak-to-peak potential (ΔE) separation for both the sensors with and without antibodies and BSA are calculated as 0.2514 and 0.2364 V, respectively. The high ΔE of the sensor with antibodies and BSA indicates a sluggish electron transfer from the electrolyte to an electrode.[39] BSA molecules are negatively charged which plays an important role to repel the ferro/ferricyanide ions from the electrode interface.[40] The BSA coating on the 3D rGO-Au microelectrode sensor also increases the selectivity of the sensor by preventing the non-specific interactions.[41] After these electrochemical characterizations, the sensor was further calibrated with different concentrations of spike S1 proteins.

4.2. Sensor Calibration with SARS-CoV-2 Spike Protein

The impedance spectroscopy was used as a sensing modality to detect the SARS-CoV-2 spike proteins in this work. This method performs rapid sensing of SARS-CoV-2 spike protein and does

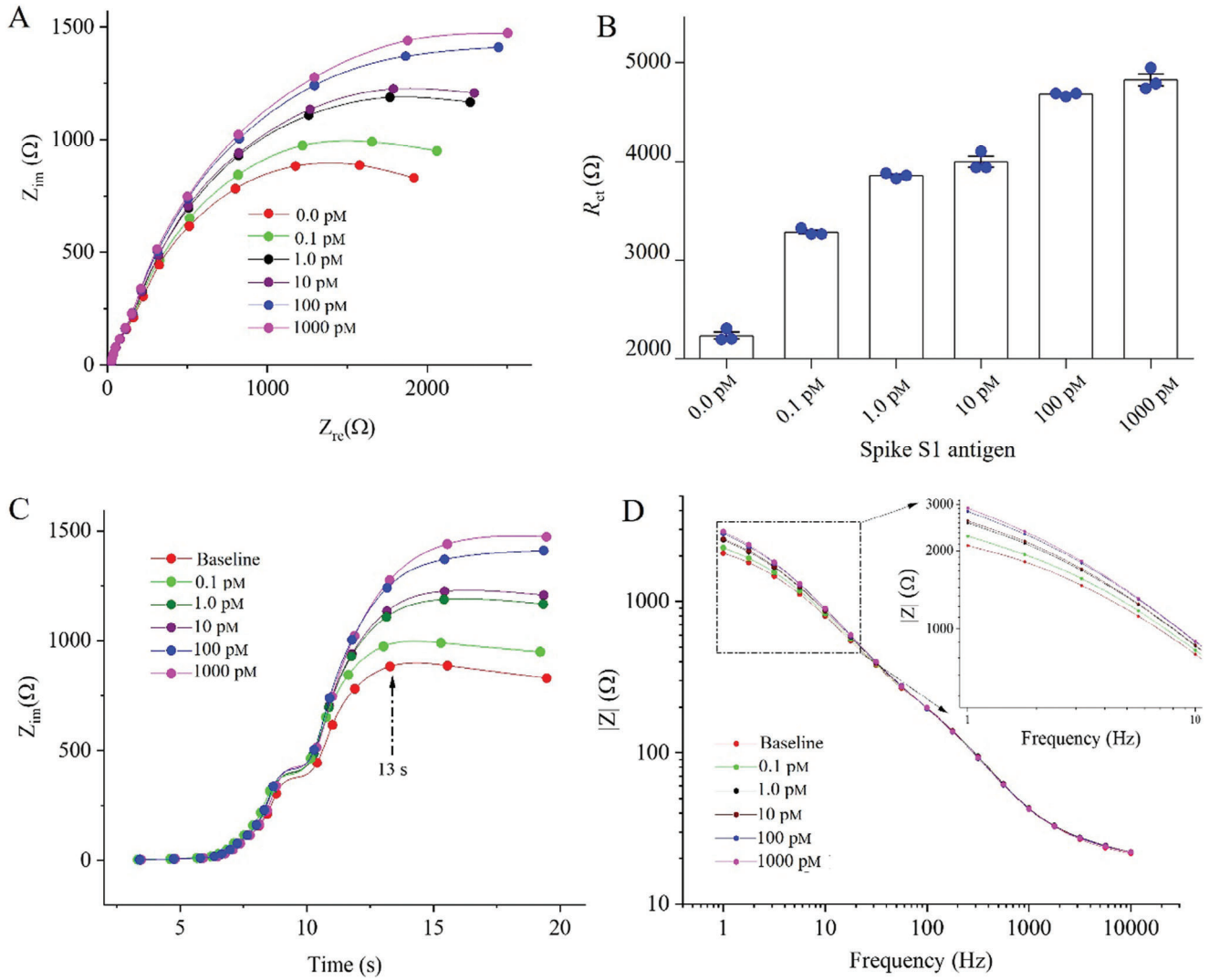

Figure 4. SARS-CoV-2 sensor calibration studies. A) Sensing results with different concentrations of SARS-CoV-2 spike S1 antigens. Sensing of SARS-CoV-2 antigens was conducted using EIS measurements. The Nyquist plots of the SARS-CoV-2 antigen sensor (A) were recorded as a function of S1 antigen at 0.1–1000 pM. B) Their corresponding R_{ct} values are plotted with respect to the different S1 antigen concentrations. In Nyquist plots, the deviation of fitted (shown in Figure 3C) and raw semicircles was less than ±3.0%. A *p*-value of <0.0001 indicates a statistically significant difference (B). C) Imaginary impedances (Z_{im}) of the sensors at different antigen concentrations were plotted against detection time in seconds. D) Modulus of impedance (|Z|) is plotted against frequency at different concentrations. Three repeated measurements were recorded for each antigen concentration. All EIS experiments for sensing antigens were recorded by applying an AC signal with an amplitude of 1 mV and a frequency range of 10 000–1 Hz. The PBS (50 mM) solution mixed with a ferro/ferricyanide (5 mM) mediator was used to prepare the titrate concentration of spike S1 antigens.

not require any labeling reagents. Other major benefits of this impedance-based sensor are ease of miniaturization and customizability, low cost, and label-free operation. This sensor measures the electrical impedance of an electrode interface in an alternative current (AC) steady state with constant direct current (DC) bias conditions. For sensing experiments, we have applied a small sinusoidal voltage (≈1 mV) with a range of frequency (1-10 000 Hz) to measure the target protein. When the target molecule (SARS-CoV-2 spike protein) is captured by the 3D electrode, the change of interface (electrode–electrolyte) impedance was detected by a potentiostat. Further, the sensing data of the EIS tool has been analyzed by fitting an equivalent circuit shown in Figure 3B.

Sensing graphs of SARS-CoV-2 antigen are shown in **Figure 4**. The titrate concentrations of spike protein were prepared in buffer solution from 0.1 to 1000 pM. A baseline measurement of the R_{ct} was set to 2.55 kΩ in presence of only buffer solution without any spike protein (Figure 4A). When a target protein (0.1 pM) was introduced the R_{ct} was increased to 3.29 kΩ compared to the baseline. This increment of R_{ct} with a minute concentration of target antigen is due to the capture of antigen on the sensor surface which blocks the electron transfer. The sensor was washed with PBS buffer before we introduced the 2nd concentration of the antigen. We have introduced a set of other antigen concentrations such as 1, 10, 100, and 1000 pM and run the EIS experiments. While the concentration of antigens was increased,

Table 1. Comparison of the performance of our 3D printed biosensor in sensing of the SARS-CoV-2 spike protein with reported literature.

Sensor materials	Detection modality	LoD	Analytical Sensitivity	Test range	Detection time (includes incubation time)
Paper-based electrochemical platform[46]	Square-wave voltammetry	12.7 pM	51 fM	38.3–76.6 fM	30 min
Functionalized TiO_2 Nanotubes[45]	Amperometry	0.07 nM	14 nM	14–1400 nM	1 min
Commercial screen-printed electrode[43]	Impedance	9.33 pM	13.3 nM	13.3–133 nM	40 min
Laser-scribed graphene[34d]	Pulse voltammetry	38.6 fM	66.6 fM	66.6 fM–6.6 pM	60 min
Screen-printed carbon electrode[47]	Square wave voltammogram	8.5 fM	21.2 fM	21.2 fM–2.1 pM	15 min
rGO-modified screen-printed carbon electrode[44]	Pulse voltammetry	10 nM	1 nM	1–60 nM	60 min
Silver nanostructures[48]	Plasmonic	9.7 fM	100 fM	100 fM–100 pM	20 min
3D microelectrode (this work)	Impedance	9.2 fM	0.1pM	0.1–1000 pM	43 s

the R_{ct} increased with each high concentration. The R_{ct} values obtained from Nyquist plots of the EIS measurements are plotted with respect to the different concentrations of spike protein (Figure 4B). The charge transfer resistance is directly proportional to the antigens. This sensor provided a detection time of 43 s (Figure 4C), wherein the sensor impedance is become saturated with 95% enhanced signal during sensing of antigens compared to the baseline. The modulus of impedance |Z| of the sensor is plotted against the logarithm of frequency (Figure 4D). As set the detection frequency from 10 000 to 1 Hz, the enhancement of impedance was seen from 100 to 1 Hz. At 1.0 Hz, the change of sensor output is shown to be maximum with the target antigen.

The analytical sensitivity of the 3D sensor is found to be 100 fM. A limit-of-detection (LoD)[42] is calculated as 9.2 fM (calculation is shown in Section S1, Supporting Information) within the range of 0.1–1000 pM concentration of antigen. The sensor calibration is shown in Figure S1A (Supporting Information). **Table 1** shows the sensing performance of the 3D microelectrode-based biosensing platform when compared to reported literature for the SARS-CoV-2 spike protein. An analogous limit-of-detection was seen with the conventional sensing materials such as screen printed electrodes,[43] rGO coated screen printed electrode,[44] laser-script graphene,[34d] titanium dioxide nanotube[45] and paper-based[46] sensing platforms (see Table 1). A faster detection system (30 s) for COVID-19 was realized when the titanium dioxide nanotube[45] was used as a sensing material for the detection of antigen. However, their limit-of-detection and analytical sensitivity (0.07–14 nM) of the target analyte are moderate.[45] When the rGO sheets were coated on a planar screen printed electrode,[44] the sensor showed a detectivity within a range of 1–60 nM, an LoD of 10 nM and a detection of time of 60 min. Our 3D sensor exhibits an excellent sensing performance such as it shows a detection time of 43 s and an LoD of 9.2 fM due to the 3D micropillar array of rGO-Au electrodes. The 3D electrode enhances not only the electrochemical reactivity due to high surface area but also provided a scaffold of multi-length-scale electrode.[28a] The multi-length-scale rGO-Au electrode offers a high surface area at the nanoscale and its micropillar geometry accelerates the interaction of diffusing target recombinant antigens even at low concentrations.[28a] Thus, our sensor is capable of detecting an ultralow concentration of spike protein within 43 s. With these excellent features, the 3D microelectrode sensor was tested on SARS-CoV-2 VOCs.

4.3. Sensing of SARS-CoV-2 VOCs

Once the sensor was calibrated with recombinant spike S1 protein, it was evaluated for the detection of spike proteins from SARS-CoV-2 VOCs. Most of the traditional diagnostic biosensors are not capable detecting SARS-CoV-2 VOCs.[49] In this study, we have prepared pseudoviruses of five types of VOCs including WT, Alpha, Beta, Gamma and Delta.[50] While there divergences among these VOCs, they still share some similarity.

The EIS sensing performance of the sensor with these variants is shown in **Figure 5A–D**. In this measurement, the sensor was set to a baseline without any pseudoviruses (Figure 5A), wherein the sensor R_{ct} is found to be at 4 kΩ. With VSV pseudovirus (R_{ct} ≈4.2 kΩ) and Mock (R_{ct} ≈4.0 kΩ) controls, the sensor doesn't show a significant change in the impedance value compared to the baseline (Figure 5B) signal. As these controls do not have specific antigens that can be captured by the antibodies on the sensor surface, the sensor doesn't show any change of impedances as evident by their larger *p*-value (*0.049*). When the sensor was exposed to the pseudoviruses of SARS-CoV-2 variants, the sensor showed higher impedances (R_{ct}). The Nyquist plots and R_{ct} values for all the variants are shown in Figure 5A,B. This sensor showed a positive response with all SARS-CoV-2 variants. Compared to the baseline and controls, the sensor responses with the variants are high and show a *p*-value less than 0.0001, which is statistically significant (Figure 5B). Sensor showed a maximum response with the WT SARS-CoV-2 and the Alpha variant. This may be due to the high affinity of the antibodies to WT and the Alpha variant. The 3D printed sensor exhibited lower responses with other SARS-CoV-2 VOCs such as Delta, Beta and Gamma compared to WT and alpha variants. This *all-in-one* versatile detection platform is attributed due to the 3D scaffold platform which allows high loading of spike antibodies throughout the sidewall of micropillars. The Bode plots show the change of magnitude of impedance and phase as a function of frequency for the detection of the SARS-CoV-2 VOCs (Figure 5C). At low

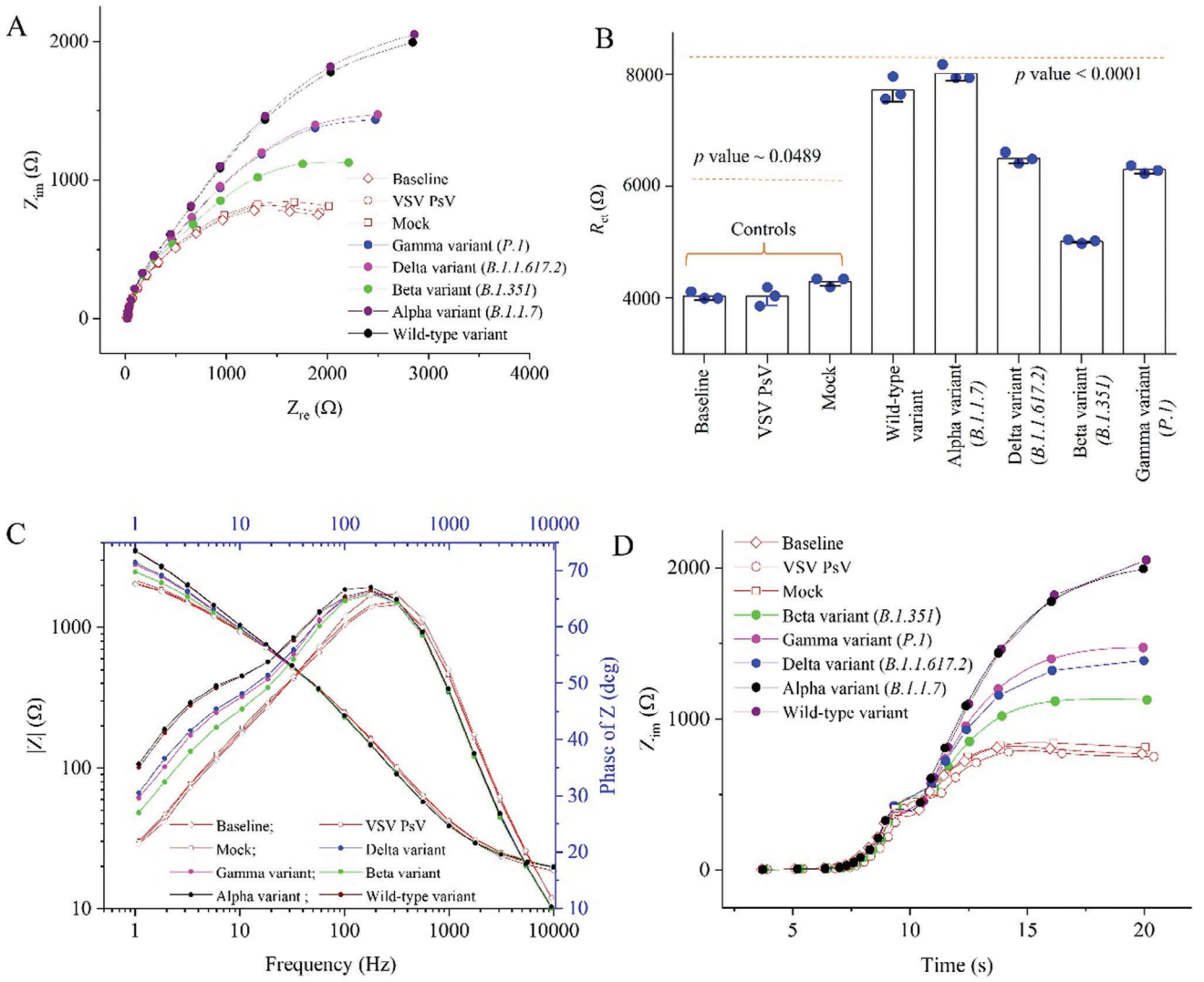

Figure 5. Sensing of SARS-CoV-2 VOCs. Based on titration measurements in Figure 4, the sensor was used to measure SARS-CoV-2 VOCs at identical conditions. A) The preparation of different SARS-CoV-2 pseudoviruses is demonstrated in Figure 1 and tested with the sensor using EIS measurement. For this study, VSV and Mock are taken as controls. WT, Alpha, Beta, Delta and Gamma are the five VOCs used in this study. B) Corresponding R_{ct} values are calculated for both controls and VOCs and plotted to evaluate *p*-value (<0.0001). For each virus and control, the sensor was run at least three repeated times. C) The detection phase and modulus of impedance are plotted with frequency for each EIS measurement. D) The Z_{im} of the sensors for detecting different VOCs were plotted against detection time in seconds. EIS measurements for sensing antigens were recorded by applying an AC signal with an amplitude of 1 mV and a frequency range of 10 000–1 Hz. The PBS (50 mM) solution mixed with a ferro/ferricyanide (5 mM) was used to prepare different concentrations of recombinant spike S1 antigens.

frequencies from 10 to 1 Hz, the change of magnitude of impedances is distinguishable with the SARS-CoV-2 VOCs. Further, the Bode phase plot for the microelectrode sensor showed the capacitive behavior caused by binding events of VOCs to the sensor surfaces at low frequencies.[51] The 3D microelectrode-based sensor showed a short detection time of 43 s (Figure 5D) for detecting SARS-CoV-2 VOCs. The short detection time is due to the reduction of diffusion length of the target antigens from bulk to the micropillar electrode.[28a]

Based on the calibration curve (shown in Figure S1, Supporting Information), the levels of antigens are calculated and plotted (Figure S2, Supporting Information). The sensor showed a molar concentration level (high) with WT and alpha variants. The high concentration may be due to the high number of antigens expressed by the plasmid. However, the sensor showed a micromolar range of concentration with Beta, Gamma and Delta variants. These results indicate that the sensor has a high ability to detect different types of SARS-CoV-2 VOCs. This inherent multiplex sensing ability of the single unit-based sensor can thus eliminate the traditional multiplex sensing with many sensor units.[52]

4.4. Specificity and Reproducibility Analysis

Specificity is one of the key parameters of the biosensor characterization, especially for the biosensing of target antigens or

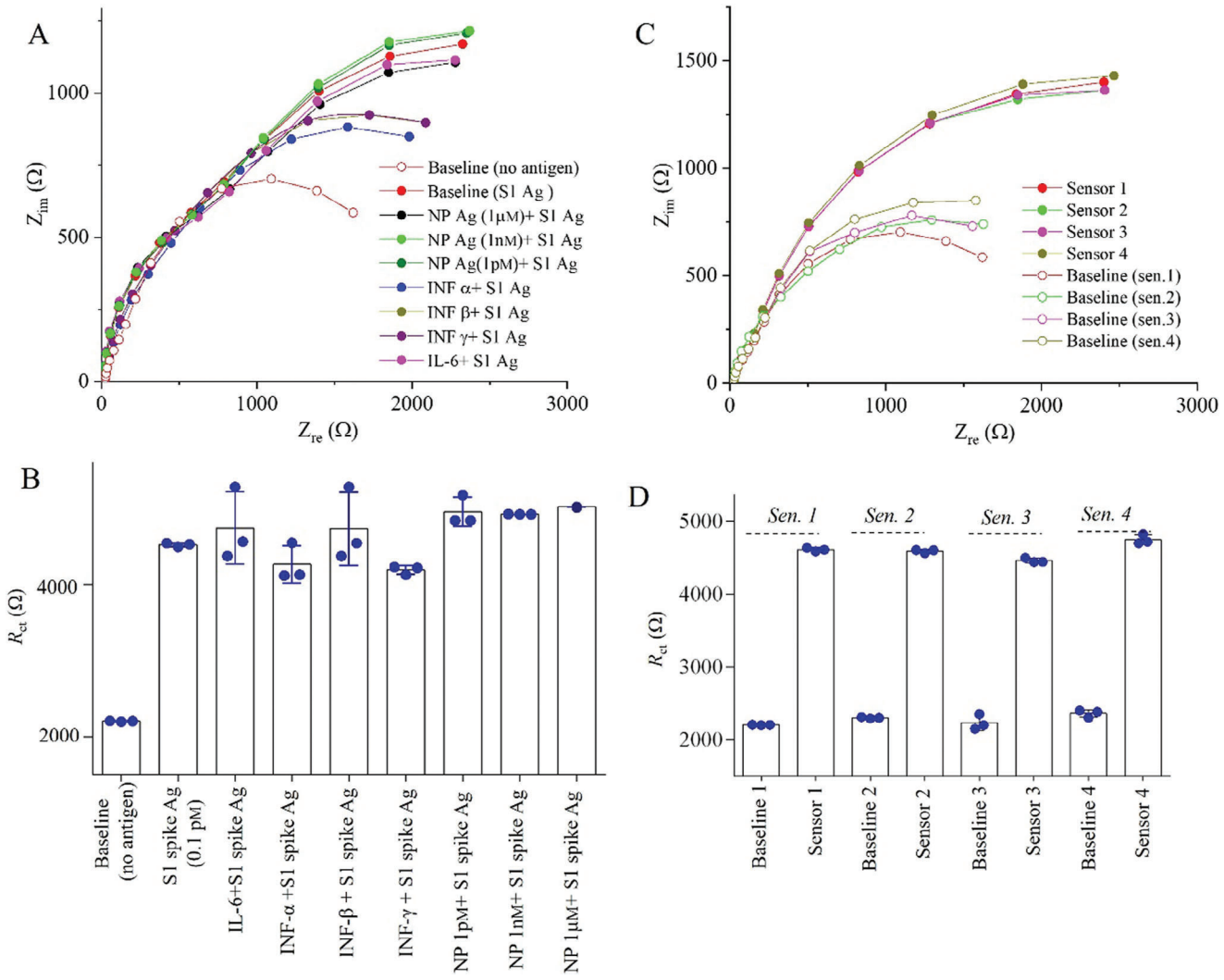

Figure 6. Sensor selectivity and reproducibility. The selectivity studies of the sensor is in presence of different antigens such as IFNs, IL-6, and NC with and without SARS-CoV-2 spike antigen (0.1 pM). The concentration of all interfering antigens is set to 10 pM. The baseline of the sensor is set at 0.1 pM concentration of SARS-CoV-2 S1 antigens. Individual interfering antigens are then added to this solution at a 1:1 ratio. A) Nyquist plots of the sensor with different interfering antigens, and B) their corresponding R_{ct} values calculated by fitting the impedance graphs in (A). C) Nyquist plots of four identical sensors tested in the same buffer solution mixed with SARS-CoV-2 antigens (0.1 pM), and D) their corresponding R_{ct} values. *p*-values were obtained as < 0.0001 when the sensors were compared with the baseline response. The PBS (50 mM) solution mixed with a ferro/ferricyanide (5 mM) mediator was used for the studies shown in this figure.

proteins due to occurrence of false readings. **Figure** 6A,B shows the specificity of the sensor in presence of possible interfering antigens from human samples including IFNs, IL-6 and SARS-CoV-2 nucleocapsid (NC). For this test, we chose a low concentration (≈0.1 pM) of SARS-CoV-2 spike antigen while the concentration of all interfering antigens was chosen as 10 pM. The baseline of the sensor was set to 2.2 kΩ of R_{ct} by exposing only buffer solution (Figure 6B). This R_{ct} value of the sensor is increased by more than double (≈4.5 kΩ) when the sensor is exposed with a minute concentration of spike S1 antigen (0.1 pM). This change of impedance is realized due to the selective capture of the target antigen. A ±3.6% of relative standard deviation (RSD) of the sensor was found when the sensor was tested with multiple interferents such as IFN-*α*, -*β* and -*γ* compared to the baseline. Similarly, the sensor showed an RSD of ±3.5% with IL-6. Further, three different concentrations (1 pM, 1 nM, and 1 μM) of an interfering antigen such as SARS-CoV-2 NC were chosen to evaluate the cross-reactivity of the sensor. With these concentrations of NC, the sensor showed an RSD of ±2.3% compared to the baseline signal. The low RSD value of the 3D microelectrode sensor indicates that the sensor does not show any reactivity with other proteins, representing good specificity for the biosensor. The 3D microelectrode geometry of the sensor may adsorb a high amount of BSA molecules which repel the non-specific antigens or proteins due to their identical surface charges (negative) as that for BSA.

The sensor-to-sensor variation is carried out to evaluate the sensor reproducibility. In this study, four identical sensors were chosen and tested in presence of SARS-CoV-2 antigen (0.1 pM) at the same buffer solution. The reproducibility results of the sensors are shown in Figure 6C,D. The baseline R_{ct} of a sensor

was found as 2.2 kΩ without any antigen. All sensors have similar results when tested against SARS-CoV-2 antigens (0.1 pM), showing an R_{ct} of 4.6 kΩ. A low deviation of 2.43% of R_{ct} is observed amongst the four sensors. For the four identical sensors, the baseline signals are very close to each other as evidenced by their low relative standard deviation of 3.5%. This high reproducibility of our sensing platform is likely due to the unique 3D hierarchical electrode geometry (microelectrode array) produced by the aerosol jet nano-manufacturing technique.

4.5. Incubation Time and Stability Analysis

To evaluate the incubation time of the sensor, we chose a specific concentration of 1 pM of SARS-CoV-2 spike S1 antigens. The incubation times for the sensor were set from 10 to 240 s and the impedimetric responses were recorded (see Figure S2A,B, Supporting Information). The Nyquist plots for the detection of antigens for different incubation times are shown in Figure S2A, while the sensor R_{ct} versus incubation times (s) of the corresponding measurements are shown in Figure S2B. We notice that the sensor provided a significant detectable signal within 10 s. After 30 s, the signal became maximum, and the sensor provided a saturated signal within 60s. Thus, 30s was chosen as the incubation time for all sensing measurements. We note that most of the sensors based on 2D materials including those with screen printed electrodes (SPE) have longer incubation times.[43,53] Introducing an array of 3D micropillars in a confined microfluidic channel may reduce the diffusion length of target molecules to be detected, and hence a short incubation time for the sensor.[54] In addition to incubation and detection times, the time cost (≈30 min) for sample collection and purification from patients may need to be considered.[48]

Our sensor shows good stability at the storage temperature of 4 °C as evidenced by the stability measurements depicted in Figure S2C,D (Supporting Information). The sensor stability test was conducted at 100 pM concentration of SARS-CoV-2 spike S1 antigens at a regular interval of 3 days. After 9 days of measurements, the sensor signal is within 10% of the initial signal. It is expected that the high surface area of micropillar array holds more BSA molecules which help reduce their bio-fouling with proteins and other contaminants, resulting in the observed good stability of the sensor.[41]

5. Discussion

The EIS method is a label-free sensing modality for rapid detection of viral infection including SARS-CoV-2 and it's VOCs.[55] The event of surface binding, mainly occurring due to antibody–antigen interactions, can be tracked by the EIS method without any labeling agents. Further, the binding event can be realized quickly, thus, rapid detection of target molecules is possible. Sensor geometry, however, can play a key role to expedite molecular events and detection. The 3D geometry of the sensor can accelerate the binding event by reducing diffusion length from the bulk solution to the electrode surface.[28a] In addition, a multi-length-electrode (combination of 3D gold microelectrode and graphene) is another key aspect to enhance electrochemical detection event of immunoreaction as evidenced by reported literature compared to a 2D electrode sensor.[28a,29] This feature of a biosensor allows a high sensitivity of a target biomarker.

The SARS-CoV-2 pseudotyped viruses could be used as alternatives for studying SARS-CoV-2 without biosafety level 3 laboratories.[17b] Further, pseudoviruses of SARS-CoV-2 VOCs can be generated and used to evaluate the sensing performance based on this work.

The sensor is calibrated with the target SARS-CoV-2 spike antigens. Specific antibodies were coated on the 3D microelectrode surface to directly capture the target antigens and change the impedance signals due to changes in the dielectric properties of the sensor. The impedance of the sensor increases with increasing concentration of the target, and the analytical sensitivity of the 3D sensor is found to be 100 fM. The sensor also shows a limit-of-detection of 9.2 fM. The 3D microelectrode array not only improves the electrochemical reactivity due to high surface area but also offers a multi-length-scale electrode geometry which significantly enhances the probability of interaction between the analyte molecules with the electrode.[28a] These features lead to a high sensitivity and a low LoD.[28a] Another important feature of this sensor is the detection of the low concentration of viral recombinant spike proteins in mere 33 s. Table 1 summarized the results of our sensor in comparison with other sensing modalities. We note that a detection time of about a minute was reported by Vadlamani et al.,[45] but at a moderate analytical sensitivity of 14 nM. Other impedance-based immunosensors also described the study of incubation time of about a minute (detection time was not mentioned) with an analytical sensitivity of about 20 pM.[56,57] In our sensor, the synergistic effect of multi-length-scale-electrode geometry of gold microelectrode array and the nanostructuring of the surface plays a key role to capture target proteins quickly and hence a saturated signal within less than a minute of incubation. There is no commercial sensor available that can detect SARS-CoV-2 within the short period reported in this work.

Several other possibilities can arise from the results presented in this work. Multiplexed sensing with a single unit-based sensor can be fabricated which can eliminate the need for multiplexing through multiple sensing units.[52] Rapid detection of viral antigens, multiplexed detection in a single sensor unit, low LoD, high specificity, reproducibility, and high sensitivity are thus the important feature of the 3D biosensing platform presented in this work. This technology represents a powerful dianostic tool in combating current and future pandemics caused by pathogens.

6. Conclusion

An ultra-rapid sensitive healthcare sensing platform that detects proteins on SARS-CoV-2 VOCs is developed in this work. The sensor is constructed by attaching suitable antibodies to aerosol jet 3D nanoprinted micropillars that form its working electrode and shows excellent performance for the detection of the SARS-CoV-2 VOCs. The unique features of this sensor platform are multiplex sensing of the SARS-CoV-2 VOCs in a single sensing unit, thus, reducing the cost per test. Unlike traditional diagnostic tools, high analytical sensitivity (100 fM), high specificity (RSD ≈ ± 3.5% with interfering proteins), and a low limit of detection (9.2 fM) are important features of this biosensor. This excellent

sensor performance is enabled by the synergistic effect of multi-length-scale-electrode geometry of gold microelectrode array and the nanostructuring of the surface using graphene. Further, this sensor has enhanced selectivity due to the microporous textured surface of the micropillar array electrode which promotes enhanced adhesion of BSA molecules, resulting in blocking of non-specific targets. This generic 3D healthcare sensing platform may allow the detection of other biomarkers such as interleukins, IFNs and other viral infections. This device could be useful to combat the continuous SARS-CoV-2 outbreaks caused by VOCs.

Supporting Information

Supporting Information is available from the Wiley Online Library or from the author.

Acknowledgements

The authors gratefully acknowledge partial financial support from the NIH BRAIN Initiative R01 award #RF1NS110483 and NSF award #CMMI-1757117. The authors acknowledge use of the Materials Characterization Facility at Carnegie Mellon University, supported by grant MCF-677785.

Conflict of Interest

The authors declare no conflict of interest.

Author Contributions

Md. A.A. and G.F.Z. contributed equally to this work. R.P. and S.-J.G came up with the concept and directed the research. Md. A.A. built the device. G.F.Z. and Md. A.A. carried out all the antibody detection tests. Md. A.A., G.F. Z., R.P., and S.-J.G. co-wrote the paper. C.H. and B.Y. carried out the AJ printing of the micropillar electrodes. C.H. and B.Y. gave inputs to the manuscript.

Data Availability Statement

The data that support the findings of this study are available from the corresponding author upon reasonable request.

Keywords

3D biosensor, nano-bio-interfaces, nanoprinting, pseudovirus, ultrarapid diagnosis, variants of concern

Received: January 10, 2024
Published online: March 12, 2024

[1] N. Nathanson, in *Viral Pathogenesis*, 3rd Ed., (Eds: M. G. Katze, M. J. Korth, G. L. Law, N. Nathanson), Academic Press, Boston **2016**.
[2] a) R. Kalkeri, Z. Cai, S. Lin, J. Farmer, Y. V. Kuzmichev, F. Koide, *Microorganisms* **2021**, *9*, 1744; b) B. Roy, J. Dhillon, N. Habib, B. Pugazhandhi, *J. Biomed. Sci.* **2021**, *8*, 8.
[3] a) C. M. Ackerman, C. Myhrvold, S. G. Thakku, C. A. Freije, H. C. Metsky, D. K. Yang, S. H. Ye, C. K. Boehm, T.-S. F. Kosoko-Thoroddsen, J. Kehe, *Nature* **2020**, *582*, 277; b) J. S. Wang, D. Y. Zhang, *Nat. Chem.* **2015**, *7*, 545.
[4] P. Muench, S. Jochum, V. Wenderoth, B. Ofenloch-Haehnle, M. Hombach, M. Strobl, H. Sadlowski, C. Sachse, G. Torriani, I. Eckerle, *J. Clin. Microbiol.* **2020**, *58*, 01694.
[5] B. Meyer, G. Torriani, S. Yerly, L. Mazza, A. Calame, I. Arm-Vernez, G. Zimmer, T. Agoritsas, J. Stirnemann, H. Spechbach, *Clin. Microbiol. Infect.* **2020**, *26*, 1386.
[6] S. Yadav, M. A. Sadique, P. Ranjan, N. Kumar, A. Singhal, A. K. Srivastava, R. Khan, *ACS Appl. Bio Mater.* **2021**, *4*, 2974.
[7] Q. Wu, C. Suo, T. Brown, T. Wang, S. A. Teichmann, A. R. Bassett, *Sci. Adv.* **2021**, *7*, eabe5054.
[8] T. Zhang, R. Deng, Y. Wang, C. Wu, K. Zhang, C. Wang, N. Gong, R. Ledesma-Amaro, X. Teng, C. Yang, *Nat. Biomed. Eng.* **2022**, *6*, 957.
[9] D. Xiong, X. Zhang, M. Shi, N. Wang, P. He, Z. Dong, J. Zhong, J. Luo, Y. Wang, J. Yu, *Microbiol. Spectr.* **2022**, *10*, 01438.
[10] a) J. Dinnes, J. J. Deeks, S. Berhane, M. Taylor, A. Adriano, C. Davenport, S. Dittrich, D. Emperador, Y. Takwoingi, J. Cunningham, S. Beese, J. Domen, J. Dretzke, L. Ferrante di Ruffano, I. M. Harris, M. J. Price, S. Taylor-Phillips, L. Hooft, M. M. Leeflang, M. D. McInnes, R. Spijker, A. Van den Bruel, C.-D. T. A. G. Cochrane, *Cochrane Database Syst. Rev.* **2021**, *3*, CD013705; b) V. M. Corman, V. C. Haage, T. Bleicker, M. L. Schmidt, B. Mühlemann, M. Zuchowski, W. K. Jo, P. Tscheak, E. Möncke-Buchner, M. A. Müller, A. Krumbholz, J. F. Drexler, C. Drosten, *Lancet Microbe* **2021**, *2*, e311.
[11] K. Tao, P. L. Tzou, J. Nouhin, R. K. Gupta, T. de Oliveira, S. L. Kosakovsky Pond, D. Fera, R. W. Shafer, *Nat. Rev. Genet.* **2021**, *22*, 757.
[12] a) W. W.-W. Hsiao, N. Sharma, T.-N. Le, Y.-Y. Cheng, C.-C. Lee, D.-T. Vo, Y. Y. Hui, H.-C. Chang, W.-H. Chiang, *Anal. Chim. Acta* **2022**, *1230*, 340389; b) A. A. Al-Fattah Yahaya, K. Khalid, H. X. Lim, C. L. Poh, *Viruses* **2023**, *15*, 624.
[13] a) B. Zeng, L. Gao, Q. Zhou, K. Yu, F. Sun, *BMC Med.* **2022**, *20*, 200; b) I. H. Hassine, *Rev. Med. Virol.* **2022**, *32*, e2313.
[14] a) N. G. Davies, S. Abbott, R. C. Barnard, C. I. Jarvis, A. J. Kucharski, J. D. Munday, C. A. Pearson, T. W. Russell, D. C. Tully, A. D. Washburne, *Science* **2021**, *372*, eabg3055; b) N. G. Davies, C. I. Jarvis, W. J. Edmunds, N. P. Jewell, K. Diaz-Ordaz, R. H. Keogh, *Nature* **2021**, *593*, 270.
[15] G. Vaidyanathan, *Nature* **2021**, *593*, 321.
[16] a) A. Y.-K. Thye, J. W.-F. Law, P. Pusparajah, V. Letchumanan, K.-G. Chan, L.-H. Lee, *Biomedicines* **2021**, *9*, 1303; b) G. F. Zhang, W. Meng, L. Chen, L. Ding, J. Feng, J. Perez, A. Ali, S. Sun, Z. Liu, Y. Huang, *J. Med. Virol.* **2022**, *94*, 5678.
[17] a) X. Deng, M. A. Garcia-Knight, M. M. Khalid, V. Servellita, C. Wang, M. K. Morris, A. Sotomayor-González, D. R. Glasner, K. R. Reyes, A. S. Gliwa, *Cell* **2021**, *184*, 3426; b) M. Chen, X.-E. Zhang, *Int. J. Biol. Sci.* **2021**, *17*, 1574.
[18] D. A. Sanders, *Curr. Opin. Biotechnol.* **2002**, *13*, 437.
[19] J. James, S. Rhodes, C. S. Ross, P. Skinner, S. P. Smith, R. Shipley, C. J. Warren, H. Goharriz, L. M. McElhinney, N. Temperton, *Viruses* **2021**, *13*, 713.
[20] a) S. Mavrikou, G. Moschopoulou, V. Tsekouras, S. Kintzios, *Sensors* **2020**, *20*, 3121; b) S. Iravani, *Mater. Adv.* **2020**, *1*, 3092.
[21] K. R. Singh, S. Rathee, G. Nagpure, J. Singh, R. P. Singh, *Mater. Lett.* **2022**, *307*, 131092.
[22] Q. Wu, W. Wu, F. Chen, P. Ren, *Analyst* **2022**, *147*, 2809.
[23] M. Alafeef, K. Dighe, P. Moitra, D. Pan, *ACS Nano* **2020**, *14*, 17028.
[24] A. Arima, I. H. Harlisa, T. Yoshida, M. Tsutsui, M. Tanaka, K. Yokota, W. Tonomura, J. Yasuda, M. Taniguchi, T. Washio, *J. Am. Chem. Soc.* **2018**, *140*, 16834.
[25] H. Li, J. Zhao, T. Wu, Z. Fu, W. Zhang, Z. Lian, S. Cai, R. Yang, *Sens. Actuators, B* **2023**, *376*, 132970.
[26] W. S. Chan, C. H. Au, H. Y. Lam, C. L. N. Wang, D. N.-Y. Ho, Y. M. Lam, D. K. W. Chu, L. L. M. Poon, T. L. Chan, J. S.-T. Zee, *Virol. J.* **2020**, *17*, 183.

[27] E. N. Özmen, E. Kartal, M. B. Turan, A. Yazıcıoğlu, J. H. Niazi, A. Qureshi, *Mater. Sci. Eng., C* **2021**, *129*, 112356.
[28] a) M. A. Ali, C. Hu, B. Yuan, S. Jahan, M. S. Saleh, Z. Guo, A. J. Gellman, R. Panat, *Nat. Commun.* **2021**, *12*, 7077; b) M. A. Ali, G. F. Zhang, C. Hu, B. Yuan, S. Jahan, G. D. Kitsios, A. Morris, S. J. Gao, R. Panat, *J. Med. Virol.* **2022**, *94*, 5808.
[29] M. A. Ali, C. Hu, S. Jahan, B. Yuan, M. S. Saleh, E. Ju, S.-J. Gao, R. Panat, *Adv. Mater.* **2021**, *33*, 2006647.
[30] a) F. Zhang, W. Li, J. Feng, S. Ramos da Silva, E. Ju, H. Zhang, Y. Chang, P. S. Moore, H. Guo, S. J. Gao, *J. Med. Virol.* **2021**, *93*, 6671; b) G. F. Zhang, W. Meng, L. Chen, L. Ding, J. Feng, J. Perez, A. Ali, S. Sun, Z. Liu, Y. Huang, H. Guo, S. J. Gao, *J. Med. Virol.* **2022**, *94*, 5678.
[31] M. Yuan, D. Huang, C. D. Lee, N. C. Wu, A. M. Jackson, X. Zhu, H. Liu, L. Peng, M. J. van Gils, R. W. Sanders, D. R. Burton, S. M. Reincke, H. Prüss, J. Kreye, D. Nemazee, A. B. Ward, I. A. Wilson, *Science* **2021**, *373*, 818.
[32] G. F. Zhang, W. Meng, L. Chen, L. Ding, S. Sun, X. Wang, Y. Huang, H. Guo, S. J. Gao, *J. Med. Virol.* **2023**, *95*, 28437.
[33] a) P. K. Sharma, E.-S. Kim, S. Mishra, E. Ganbold, R.-S. Seong, A. K. Kaushik, N.-Y. Kim, *ACS Sens.* **2021**, *6*, 3468; b) M. A. Mujawar, H. Gohel, S. K. Bhardwaj, S. Srinivasan, N. Hickman, A. Kaushik, *Mater. Today Chem.* **2020**, *17*, 100306.
[34] a) J. Sengupta, C. M. Hussain, *Carbon Trends* **2021**, *2*, 100011; b) V. Palmieri, M. Papi, *Nano Today* **2020**, *33*, 100883; c) S. Afroj, L. Britnell, T. Hasan, D. V. Andreeva, K. S. Novoselov, N. Karim, *Adv. Funct. Mater.* **2021**, *31*, 2107407; d) T. Beduk, D. Beduk, J. I. de Oliveira Filho, F. Zihnioglu, C. Cicek, R. Sertoz, B. Arda, T. Goksel, K. Turhan, K. N. Salama, *Anal. Chem.* **2021**, *93*, 8585.
[35] a) M. A. Ali, C. Singh, K. Mondal, S. Srivastava, A. Sharma, B. D. Malhotra, *ACS Appl. Mater. Interfaces* **2016**, *8*, 7646; b) M. A. Ali, K. Mondal, Y. Jiao, S. Oren, Z. Xu, A. Sharma, L. Dong, *ACS Appl. Mater. Interfaces* **2016**, *8*, 20570; c) M. A. Ali, H. Jiang, N. K. Mahal, R. J. Weber, R. Kumar, M. J. Castellano, L. Dong, *Sens. Actuators, B* **2017**, *239*, 1289.
[36] S. Srivastava, S. Abraham, C. Singh, M. A. Ali, A. Srivastava, G. Sumana, B. D. Malhotra, *RSC Adv.* **2015**, *5*, 5406.
[37] H. S. Magar, R. Y. Hassan, A. Mulchandani, *Sensors* **2021**, *21*, 6578.
[38] M. A. Ali, K. Kamil Reza, S. Srivastava, V. V. Agrawal, R. John, B. D. Malhotra, *Langmuir* **2014**, *30*, 4192.
[39] N. Elgrishi, K. J. Rountree, B. D. McCarthy, E. S. Rountree, T. T. Eisenhart, J. L. Dempsey, *J. Chem. Educ.* **2018**, *95*, 197.
[40] K. Kubiak-Ossowska, B. Jachimska, P. A. Mulheran, *J. Phys. Chem. B* **2016**, *120*, 10463.
[41] J. Sabaté del Río, O. Y. Henry, P. Jolly, D. E. Ingber, *Nat. Nanotechnol.* **2019**, *14*, 1143.
[42] D. A. Armbruster, T. Pry, *Clin. Biochem. Rev.* **2008**, *29*, S49.
[43] A. R. Cardoso, J. F. Alves, M. F. Frasco, A. M. Piloto, V. Serrano, D. Mateus, A. I. Sebastião, A. M. Matos, A. Carmo, T. Cruz, *Mater. Today Bio* **2022**, *16*, 100354.
[44] B. A. Braz, M. Hospinal-Santiani, G. Martins, C. S. Pinto, A. J. Zarbin, B. C. Beirão, V. Thomaz-Soccol, M. F. Bergamini, L. H. Marcolino-Junior, C. R. Soccol, *Biosensors* **2022**, *12*, 885.
[45] B. S. Vadlamani, T. Uppal, S. C. Verma, M. Misra, *Sensors* **2020**, *20*, 5871.
[46] A. Yakoh, U. Pimpitak, S. Rengpipat, N. Hirankarn, O. Chailapakul, S. Chaiyo, *Biosens. Bioelectron.* **2021**, *176*, 112912.
[47] S. Eissa, H. A. Alhadrami, M. Al-Mozaini, A. M. Hassan, M. Zourob, *Microchim. Acta* **2021**, *188*, 199.
[48] N. Bhalla, A. F. Payam, A. Morelli, P. K. Sharma, R. Johnson, A. Thomson, P. Jolly, F. Canfarotta, *Sens. Actuators, B* **2022**, *365*, 131906.
[49] S. P. Otto, T. Day, J. Arino, C. Colijn, J. Dushoff, M. Li, S. Mechai, G. Van Domselaar, J. Wu, D. J. Earn, *Curr. Biol.* **2021**, *31*, R918.
[50] A. Telenti, E. B. Hodcroft, D. L. Robertson, *Cold Spring Harbor Perspect. Med.* **2022**, *12*, a041390.
[51] N. R. Shanmugam, S. Muthukumar, S. Prasad, *Sci. Rep.* **2016**, *6*, 33423.
[52] F. Jiang, Z. Xiao, T. Wang, J. Wang, L. Bie, L. Saleh, K. Frey, L. Zhang, J. Wang, *Chem. Commun.* **2022**, *58*, 7285.
[53] M.-K. Park, H. C. Wikle III, Y. Chai, S. Horikawa, W. Shen, B. A. Chin, *Food Control* **2012**, *26*, 539.
[54] M. Ali, C. Hu, B. Yuan, S. Jahan, M. S. Saleh, Z. Guo, A. J. Gellman, R. Panat, *Nat. Commun.* **2021**, *12*, 7077.
[55] a) C.-H. Chuang, M. Shaikh, C. Cheng, M. Hsu, M. Wu, in *Point of Care Diagnostics-New Progresses and Perspectives*, IAPC-OBC Publishing, Croatia **2017**; b) J. S. Daniels, N. Pourmand, *Electroanalysis* **2007**, *19*, 1239.
[56] T. A. R. Cordeiro, H. R. Martins, D. L. Franco, F. L. N. Santos, P. A. F. Celedon, V. L. Cantuária, M. de Lana, A. B. Reis, L. F. Ferreira, *Biosens. Bioelectron.* **2020**, *169*, 112573.
[57] R. M. Torrente-Rodríguez, H. Lukas, J. Tu, J. Min, Y. Yang, C. Xu, H. B. Rossiter, W. Gao, *Matter* **2020**, *3*, 1981.